Methods 214 (2023) 18–27

Contents lists available at ScienceDirect

Methods

journal homepage: www.elsevier.com/locate/ymeth

Anle138b interaction in α-synuclein aggregates by dynamic nuclear polarization NMR

Rıza Dervişoğlu [a,1,2], Leif Antonschmidt [a,2], Evgeny Nimerovsky [a], Vrinda Sant [a], Myeongkyu Kim [a], Sergey Ryazanov [a,b], Andrei Leonov [a,b], Juan Carlos Fuentes-Monteverde [a], Melanie Wegstroth [a], Karin Giller [a], Guinevere Mathies [c], Armin Giese [b], Stefan Becker [a], Christian Griesinger [a,d], Loren B. Andreas [a,*]

[a] Department of NMR Based Structural Biology, Max Planck Institute for Multidisciplinary Sciences, Göttingen, Germany
[b] Center for Neuropathology and Prion Research, Ludwig-Maximilians University, Munich, Germany
[c] Department of Chemistry, University of Konstanz, Konstanz, Germany
[d] Cluster of Excellence "Multiscale Bioimaging: From Molecular Machines to Networks of Excitable Cells" (MBExC), University of Göttingen, Göttingen, Germany

ARTICLE INFO

Keywords:
Amyloid
Membrane-protein
DNP-NMR
MAS-NMR
Drug
Small-molecule
Atomic distance
Anle138b
Alpha-synuclein

ABSTRACT

Small molecules that bind to oligomeric protein species such as membrane proteins and fibrils are of clinical interest for development of therapeutics and diagnostics. Definition of the binding site at atomic resolution via NMR is often challenging due to low binding stoichiometry of the small molecule. For fibrils and aggregation intermediates grown in the presence of lipids, we report atomic-resolution contacts to the small molecule at sub nm distance via solid-state NMR using dynamic nuclear polarization (DNP) and orthogonally labelled samples of the protein and the small molecule. We apply this approach to α-synuclein (αS) aggregates in complex with the small molecule anle138b, which is a clinical drug candidate for disease modifying therapy. The small central pyrazole moiety of anle138b is detected in close proximity to the protein backbone and differences in the contacts between fibrils and early intermediates are observed. For intermediate species, the 100 K condition for DNP helps to preserve the aggregation state, while for both fibrils and oligomers, the DNP enhancement is essential to obtain sufficient sensitivity.

1. Introduction

Alpha-synuclein (αS) aggregation [1] is associated with several neurodegenerative diseases, the most prominent being Parkinson's disease (PD), dementia with Lewy bodies and multiple system atrophy. The pathological protein deposits formed in the brain, Lewy bodies, Lewy neurites and glial cytoplasmic inclusions are rich in αS fibrils. Structure elucidation by X-ray diffraction [2] and Cryo-EM [3,4] reveals a cross-β-sheet pattern in the fibrils in which the β-strands lie approximately perpendicular to the axis of the fiber.

While the accumulation of fibrillar aggregates is one of the major pathological hallmarks of the aforementioned neurodegenerative diseases in the brain, there is now mounting evidence that intermediate species of αS fibrilization are particularly toxic [5–12]. Toxicity mechanisms have been linked to interaction with lipids such as disruption or insertion into membranes, and formation of pores that allow uncontrolled ion currents, in particular calcium influx [11,13–20].

Intrinsically disordered in solution, membrane-bound αS monomer is known to interact with lipids through formation of an N-terminal helix (Fig. 1) [21]. Oligomeric αS species then form through as yet uncharacterized nucleating structures [22], before converting into protofibrils and fibrils. We recently reported the presence of two distinct oligomeric intermediates, I and II [23]. By centrifugation and temperature reduction, aggregation can be stopped at time points that maximize the concentration of either intermediates or fibrils. In the presence of lipids, αS was shown to convert stepwise from monomer via two intermediates into fibrils [23] (Fig. 1). The lipophilic small molecule anle138b, [3-(1,3-benzodioxol-5-yl)-5-(3-bromophenyl)-1*H*-pyrazole], is a clinical

* Corresponding author.
E-mail address: land@nmr.mpibpc.mpg.de (L.B. Andreas).
[1] Max Planck Institute for Chemical Energy Conversion, Mülheim a.d. Ruhr, Germany.
[2] R.D. and L.A. contributed equally.

https://doi.org/10.1016/j.ymeth.2023.04.002
Received 30 November 2022; Received in revised form 22 March 2023; Accepted 6 April 2023
Available online 8 April 2023

candidate for treatment of diseases with characteristic build-up of fibrils, prominently those associated with αS [17,24–31]. In molecular modeling simulation, the central pyrazole of the molecule forms hydrogen bonds with the protein backbone of oligomers [32] and in mature fibrils, the molecule is found in a tubular cavity [33]. Anle138b's mode of action has been attributed to modulation of toxic oligomers [26–27]. Therefore, we are interested in studying the interaction of anle138b with such oligomeric intermediates and with fibrils in the presence of lipids.

Characterization of small molecule interaction with such species requires development of methods that can provide high resolution structure information. Previously, small molecules that interact with fibrils have been investigated via magic angle spinning (MAS) nuclear magnetic resonance (NMR) for the proteins HET-s [34,35] and Amyloid-β (Aβ) [36]. For both, the three-dimensional structure of the interface between an amyloid fibril and a small molecule was determined with atomic resolution. For HET-s fibrils, the Congo red binding site was elucidated using polarization transfer from protons of the small molecule [35]. For A β fibrils, sulindac sulfide was located based on ^{19}F REDOR [37]. For these examples, chemical shift perturbations of protein fibrils, induced from the binding of the small molecule were not sufficient to localize its binding site. Therefore, direct distance information is needed to reliably identify binding sites. In addition to NMR-based localization of small molecules, recent reports from cryo-EM have assigned densities in Tau fibrils to small molecules such as EGCG and a positron emission tomography (PET) tracer [38–39]. It is not yet clear how useful cryo-EM will be in the characterization of oligomeric species.

Detecting anle138b-protein interaction necessitates sensitive methods, because its concentration is low due to stoichiometry. A binding stoichiometry of 1:7 (anle138b: protein monomers) was found for αS fibrils exposed to anle138b in water [40], with tight binding (K_d of 190 ± 120 nM [40,41]) indicating that several protein molecules arrange to form the interaction surface. More recently, we used a combination of cryoEM and NMR to locate anle138b in a tubular cavity within the fibril [33]. This binding mode, in which the long axis of anle138b aligns with the fibril axis, finds anle138b interacting with several strands, each from different protein monomers. The periodicity of the fibril structure allowed anle138b to move along the cavity in MD simulations [33]. The stoichiometry found for preformed fibrils in the absence of lipids does not necessarily reflect the stoichiometry for fibril samples prepared in lipids, but nevertheless, is close to the expectation of 4 to 5 based only on the size of the small molecule. Such a binding mode parallel to the fibril axis is similar to the fibril binders thioflavin T (ThT) and Congo red [42–44].

At 140 residues, αS is 2–3 fold larger than proteins investigated in other fibril studies locating small molecules via NMR [34–36]. Prefibrillar and fibrillar aggregates of αS thus present a particular sensitivity challenge, that is exacerbated by dilution in lipids. Note that although the number of folded residues in αS is much less than the total, unfolded residues also take up space in the MAS NMR rotor, and thus reduce the molar concentration that can be achieved in the fibril/lipid pellet.

The combination of orthogonal labelling of the small molecule and αS in combination with dynamic nuclear polarization (DNP) enhanced solid state NMR can overcome such challenges. Nevertheless, direct detection of the small molecule-protein interaction via NMR is still challenging when the small molecule lies along the fibril axis, since a single reporter in the small molecule is present for multiple copies of the protein. This increases the effective molecular size several fold, commensurately magnifying the sensitivity challenge. This challenge was overcome by an elegant isotope labelling strategy in which the protein was deuterated, while the small molecule was not, allowing multiple protons from the small molecule to accumulate to signal detection in the fibril [35]. While the method improves sensitivity, and is atomic-resolution with respect to the protein, it is inherently no longer atomic resolution from the perspective of the small molecule. In an alternate approach, the ^{19}F moiety of a small molecule was used to probe interactions in Aβ, benefitting from the relatively far-reaching effects of the high gamma ^{19}F spin [37].

A similar sensitivity problem arises for oligomeric membrane proteins, for which the sensitivity challenge has been addressed via DNP [45]. In particular, for the Influenza A M2 protein, the drug rimantadine binds with a stoichiometry of 1:4 to protein monomers, since the drug binding site in the pore of the protein is formed from protein tetramers. Here the effective molecular weight of the system is increased from about 5 kDa to 20 kDa.

Hyperpolarization methods [46–48], such as cross effect DNP can improve the sensitivity by orders of magnitude [46,49,50]. The asymmetric biradical, TEMTriPol-1, was shown to outperform bis-nitroxide radicals for high field DNP MAS NMR, which in part is explained by lack of depolarization that can occur due to the combined effects of sample spinning and orientation dependent EPR transitions [51,52]. Recently, a more polar asymmetric biradical was introduced [53], which overcomes potential issues with aggregation or protein-polarizer interaction in biological samples, which might otherwise lead to less than ideal signal enhancement. The polarizing agents AMUPol and TOTAPOL have been investigated before in the context of biological assemblies using 10 percent deuterated DMSO [54]. In general, DNP MAS NMR at 100 K has the further advantage that the low temperature prevents changes in the sample during measurement [47–48], which is important here to prevent the conversion of intermediates into fibrils.

For this study, we prepared aggregates of αS in the presence of liposomes according to the recently described protocol [23] with anle138b present in the liposomes. Benefitting from DNP enhancement, the direct interaction between the small molecule and protein

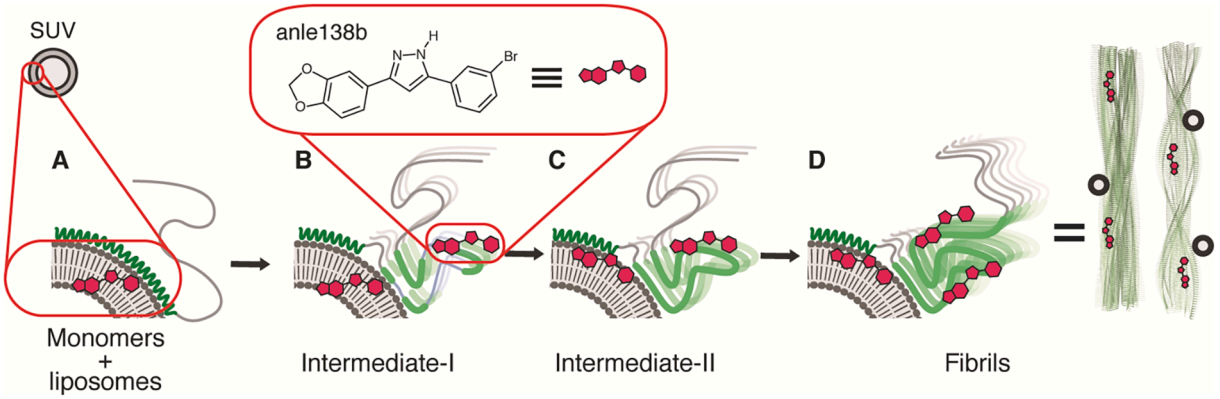

Fig. 1. Schematic illustration of the αS fibrilization pathway in the presence of anle138b and lipids (not drawn to scale). A) αS monomers with anle138b loaded lipids. B) αS Intermediate-I on lipids with anle138b. C) αS Intermediate-II on lipids with anle138b. D) αS fibrils with lipids and anle138b shown in two perspectives, one prepared using the protein data bank (PDB) structures 6cu7 and 6cu8.

aggregates is detected, both for fibrils as well as for the Intermediate-I, which has only partially formed the β sheet structure found in fibrils, and is not ThT positive.

2. Materials & methods

2.1. Preparation of αS aggregate samples

Samples of lipid vesicles as well as αS Intermediate-I and fibrils were prepared as previously reported [23]. In brief, vesicles were prepared by mixing 1-palmitoyl-2-oleoyl-*sn*-glycero-3-phosphocholine (POPC), 1-palmitoyl-2-oleoyl-*sn*-glycero-3-phosphate (POPA) (sodium salt) and anle138b in chloroform, evaporating the solvent under a N_2-stream and lyophilizing overnight. Small unilamellar vesicles (SUVs) were obtained from the lipid film by addition of buffer (50 mM HEPES, 100 mM NaCl, pH 7.4) and repeated sonication. The initial solution contained 1.5 mM POPC, 1.5 mM POPA and 150 μM anle138b. Anle138b containing vesicles were incubated with αS (70 μM, amino acid sequence in Table S3) in the buffer at a molar lipid to protein ratio of L/P = 10:1 and subjected to repeated cycles of 30 s sonication (20 kHz) at 37 °C followed by an incubation period of 30 min. Aggregation was monitored regularly by measuring ThT fluorescence and aggregates were isolated at key time points by centrifuging at 55,000 rpm (TLA-100.3 rotor in an Optima™ MAX-TL) for 1 h at 4 °C.

Anle138b was synthesised according to the published protocol [26,33].

The radical solution in ^{13}C-depleted d_8-Glycerol, D_2O and H_2O (60:30:10 vol%), namely "DNP juice", containing either 15 mM TEMTriPol or 30 mM AMUPol was added to the above described protein-lipid-aggregate resulting in an intended concentration of 4–5 mM biradical. This is substantially different from the 8 mM via EPR (Fig. S3). The discrepancy is likely due to the difficulty of accurately handling the concentrated radical solution near the solubility limit (some biradical may have precipitated in the stock solution). Low radical concentrations below about 10 mM are beneficial for long mixing time TEDOR and REDOR experiments since it improves relaxation times. This results in a lower DNP enhancement factor than can be observed with > 10 mM biradical [45,55]. The sample was mixed thoroughly with a stainless-steel needle before being centrifuged into 3.2 mm sapphire or zirconia MAS NMR rotors using a custom-made filling device made from a truncated pipette tip. Finally, the sample was further centrifuged into the rotor in an ultracentrifuge packing device for 30 min at 24,000 rpm in a SW 32 Ti rotor in an Optima™ L-80 XP Ultracentrifuge (both Beckman Coulter) [56,57]. To check the sample integrity after addition of glycerol and TEMTriPol-1 for DNP, we recorded 2D ^{13}C–^{13}C and ^{1}H-^{15}N correlations spectra of both the fibril and Intermediate-I (Figs. S8–S10) and observed characteristic oligomer or fibril peaks. The room temperature ^{1}H-^{15}N correlation spectra in Fig. S9 also reveal the limited stability of the Intermediate-I at 290 K. The list of samples used in this study is reported in Table S2.

2.2. DNP MAS NMR

All DNP spectra were recorded at a magnetic field of 14.1 T using a 600 MHz Bruker Avance III HD spectrometer, and a 3.2 mm low temperature (LT) HCN MAS probe. 395 GHz microwave irradiation from a gyrotron oscillator was delivered to the sample through a corrugated waveguide. In the Bruker gyrotron control interface, cavity temperature, collector current, and cathode voltage were optimized for best microwave output, and on the magnet side the Z_0 field was adjusted for best signal sensitivity. For the LT MAS probe, variable temperature, bearing and drive gasses were cooled with a second-generation Bruker liquid nitrogen cold cabinet, operating at 100 K. The 3.2 mm rotor was spun at 12.5 kHz (RFDR, REDOR and 2D zf-TEDOR) and 10 kHz (FS-REDOR) and ^{1}H and ^{13}C pulse powers were 83.3 kHz. The ^{1}H SPINAL-64 [58] decoupling was 83 kHz during acquisition and RFDR, while during FS-REDOR and TEDOR recoupling it was set to 100 kHz. ^{1}H–^{13}C cross-polarization (CP) was applied with a 90–100% ramp on the proton channel and for 1.5 ms for RFDR and REDOR or 2 ms for FS-REDOR. The ^{1}H-^{15}N CP was applied for 800 μs with an 80–100% ramp on the proton channel. The ^{1}H–^{13}C CP of the NHHC spectrum was set to 300 μs to transfer over only a short distance (about one bond). The 1.3 ms ^{13}C RFDR spectrum was implemented using xy-8 phase cycling and 83 kHz pi-pulses. For FS-REDOR, a series of 40 kHz π-pulses were applied on the ^{15}N channel. In the middle of the recoupling block, soft pulses with the Q3 shape [59] were applied with 1 ms duration for both the ^{13}C and ^{15}N channels. Reference (S_0) signal was acquired by switching off the soft pulse on the ^{15}N channel. The 2D zf-TEDOR hard-pulse powers for ^{1}H, ^{13}C and ^{15}N were 100 kHz, 83 kHz and 41.6 kHz respectively, using rotor synchronized z-filter duration of ~ 2.5 ms. The room temperature (300 K) experiments were recorded at 20 T with 17.5 kHz MAS also in a 3.2 mm rotor with the same pulse sequence details as described above.

2.3. Polarizing agent TEMTriPol-1

TEMTriPol-1 [52] was synthesized in the chemical synthesis facility of the Max Planck Institute for Multidisciplinary Sciences, based on published protocols [60]. The resulting bi-radical was found to actually be a mixture of bi-radical and monoradical based on EPR spectra. However, the chemical composition was intact without major impurities as observed with HPLC and UV/Vis-HPLC spectra. Accordingly, we conclude that the monoradicals in the sample are single site quenched TEMTriPol-1 radicals (Details in the SI). The DNP performance of TEMTriPol-1 was compared to AMUPol as described in the main text (Fig. S17). The standard sample of 2 mM Proline with 10 mM TEMTriPol-1 in DNP juice results in an enhancement factor of 68.

2.4. Room temperature NMR

Spectra at room temperature were recorded on 850 MHz and 800 MHz Bruker Avance III HD instruments, using a 3.2 mm HCN E-free probe and a 1.3 mm HCN probe, respectively. The spinning frequency was set to 17.5 kHz and 55 kHz respectively, and the cooling gas was set to 800 L/h and 1450L/h in order to reach a sample temperature of approximately 300 K (thermocouple reading of 290 K). Pulse powers of 100 kHz and 83.3 kHz for ^{1}H and ^{13}C channels were used respectively on the 3.2 mm probe at the 850 MHz magnet. During ^{13}C acquisition, 100 kHz SPINAL-64 [58] decoupling was applied on the ^{1}H channel. The ^{13}C RFDR spectrum was conducted with 2.9 ms mixing using 83 kHz π-pulses and 83 kHz SPINAL-64 proton decoupling. The ^{1}H–^{13}C CP was 3 ms with a 90–100 % ramp on the ^{1}H channel. With the 1.3 mm probe, pulse powers of ~ 105 kHz and 38 kHz for ^{1}H and ^{15}N channels were used to acquire (H)NH fingerprinting spectra. The acquisition time was 15 ms for ^{15}N and 42 ms for ^{1}H. The forward CP was 0.9 ms with a ramp of 80–100 on ^{1}H and back CP was 0.55 ms with a 100–80 ramp on ^{1}H. The water suppression was 13.75 kHz MISSISSIPPI [61] for 100 to 200 ms. Proton decoupling of 12.75 kHz SWf-TPPM [62] was used in the indirect dimension and 10 kHz WALTZ-16 heteronuclear decoupling [63] was applied during acquisition.

2.5. Distance calculation from REDOR spectra

REDOR dephasing curves [64] were fit to numerical simulations using in-house MATLAB code solving the equation of motion detailed in a previous publication where *J*-couplings between two labelled carbons in anle138b were also taken into account [65–67]. For simulations of frequency selective REDOR, the product of two-spin time-dependent signals was calculated, as detailed previously [68,69]. In this case, the effect of the ^{13}C–^{13}C J-coupling is removed, but all backbone nitrogen signals are assumed to be recoupled (they are all expected to be within the bandwidth of the selective pulse). The distance errors were calculated by adding or subtracting the noise level of each point in the REDOR

curve.

3. Results & discussion

To detect the interaction of anle138b with both fibrils as well as intermediate-I of αS [23], we recorded dynamic nuclear polarization (DNP) enhanced MAS NMR [46] spectra in the presence of the bi-radical TEMTriPol-1 [52]. We prepared the samples in a glass-forming matrix of glycerol-water, added TEMTriPol-1 and cooled to 100 K [48,70]. We also prepared samples with the biradical AMUPol [71] (Fig. 2, Fig. S17). The thermal signals of fibrils in the presence of AMUPol or TEMTriPol-1 differ by approximately a factor of 2 (Fig. 2, microwave (μw) = OFF), in agreement with previous publications showing that depolarization [72–74] reduces the MAS NMR signal by up to 60% in the presence of AMUPol [75], while almost no loss is observed with TEMTriPol-1 [51]. In keeping with the understanding that TEMTriPol-1 hydrophobicity can be problematic for biological samples and can cause unwanted protein-radical interaction [53,76], the enhancement values varied greatly among different preparations. Some of our preparations contained only 30 to 45 percent glycerol to limit the intensity of the glycerol carbon signals, in particular, those shown in Fig. 2A-B. With microwaves on (Fig. 2, μw = ON), the enhancement factor ($\varepsilon_{on/off}$) for both radicals under these conditions was about 8. With a glycerol concentration of about 60 percent, which better ensures glass formation during freezing, an enhancement factor of about 43 was observed for AMUPol, and 10 for TEMTriPol-1 on protein and lipid resonances, e.g. the C′ shift at 175 ppm (Fig. 2C). Note that the higher concentration of glycerol resulted in a larger glycerol background signal in this sample, and that the glycerol signal enhancement is larger than lipid and protein enhancement, which is a well-known effect in multi-phase systems [77]. In a third composition, consisting of 50% glycerol, and 2% DMSO, an enhancement factor of 23 was observed with TEMTriPol-1 (Fig. 2D). Rather than anle138b, this sample contained a diaryl pyrazole small molecule, 'compound 2' of a recent patent [78], that is structurally related to MODAG-001 [79]. The large variation in observed enhancement factors, which we believe occurs mainly due to the biradical distribution in different sample preparations, prevents a direct comparison of the two radicals from our data on membranous samples. For TEMTriPol series polarizing agents, those with improved water solubility will likely be used in the future [53,76].

Fig. S1 in the supporting information compares the sensitivity of the DNP sample at the 600 MHz DNP spectrometer at 100 K with measurement of the same sample (before addition of radical and glycerol) at an 850 MHz spectrometer without DNP at room temperature. In both, the ^{1}H–^{13}C CP spectrum is detected on ^{13}C and profits from the proton polarization, or hyperpolarization in the DNP enhanced spectrum. The sample was ^{15}N labelled αS fibrils in the presence of lipids and containing site-specific ^{13}C labelled anle138b (see Fig. 3B). The sensitivity available with DNP was found to be about 4 to 10-fold higher than at the 850 MHz instrument as measured for protein aromatic resonances, or anle138b, respectively (details in Table S1 in the SI). The improved sensitivity with DNP enhancement is critically important to measure interactions, here between anle138b and the protein, due to acceleration of the measurement by about 16 to 100-fold since sensitivity scales with the square root of measurement time; practically speaking a 4- to 7-day DNP measurements would be expected to require months of acquisition on the 850 MHz equipment. However, in this time, the intermediates start converting to fibrils (Fig. S9), and even for fibrils, the long measurement times are impractical. In some cases, structural dynamics in the bound complex may also interfere with polarization transfer. We believe that this is likely the case for anle138b bound to lipidic αS fibrils, based on MD simulations [33]. Note also that this comparison was done

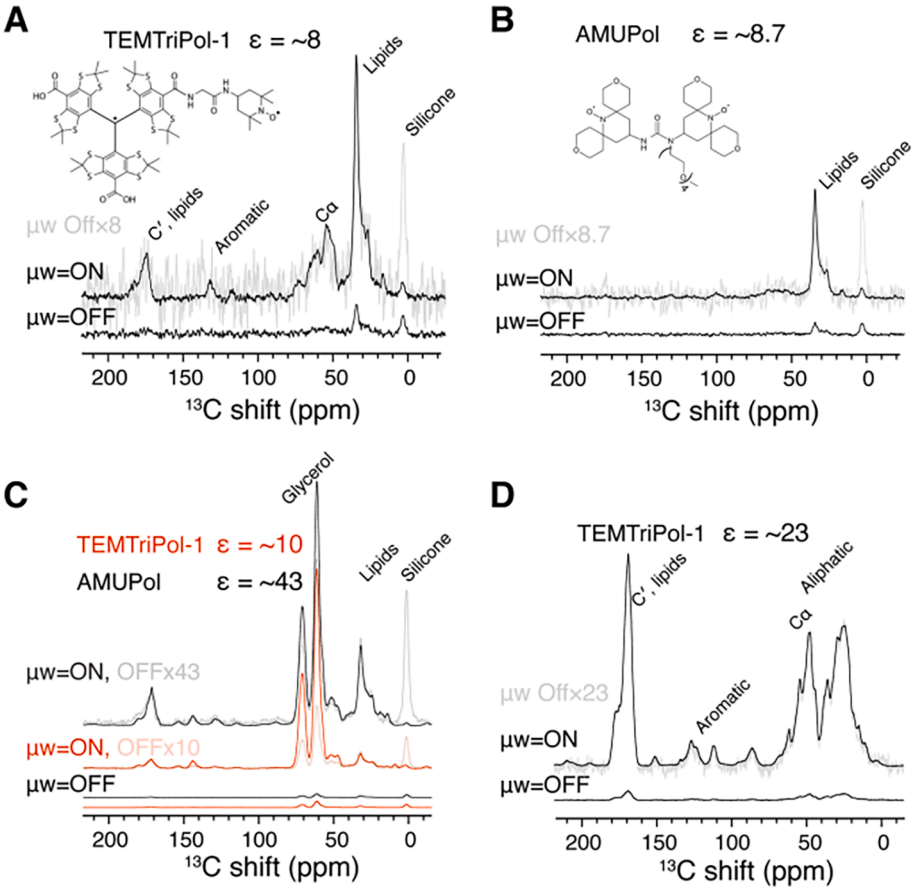

Fig. 2. DNP signal enhancement with TEMTriPol-1 (A) and AMUPol (B). Spectra obtained with microwaves off (μw = Off) are shown scaled up by the enhancement factor in grey. The chemical structure of each biradical polarizing agent is shown above the spectra. The vertical scaling is consistent in A and B, while fewer scans were averaged in A, as can be seen by the higher noise level. Samples contained about 45 percent glycerol. (C) shows another comparison of AMUPOL and TEMTriPol-1, using 60 percent glycerol. 10-fold more scans were acquired for the off signal, and the data scaled accordingly. (D) shows the microwave on and off spectra of a sample that contained 2 percent DMSO in addition to about 50 percent glycerol. Data were recorded at a temperature of 100 K at 600 MHz with 12.5 kHz MAS except in (B), which was with 8 kHz MAS. The sample was ^{15}N labelled αS fibrils (A-C) or ^{13}C labeled αS fibrils (D) grown in the presence of ^{13}C labelled anle138b (A-C) or a related pyrazole, see text (D).

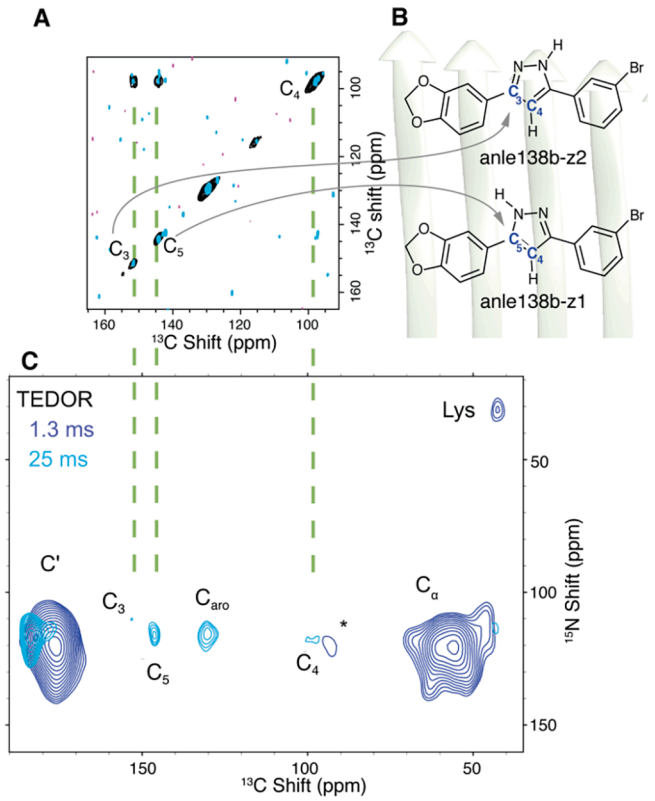

Fig. 3. Detection of close proximity between anle138b and αS aggregates. In (A) 2D ^{13}C–^{13}C RFDR spectra of ^{15}N labelled αS fibrils grown in the presence of ^{13}C labelled anle138b doped liposomes are shown measured at 850 MHz (light blue) and the same sample after addition of glycerol and TEMTriPol-1 at 600 MHz using DNP (black). The C_3-C_4 and C_5-C_4 cross-peaks of anle138b-z2 and –z1, respectively, are evident in the two-site ^{13}C-labelled molecule. Asymmetry of cross peaks can be explained by the efficiency of the CP step before t_1 that preferentially excites C_4. Signals from the fibril are detected only on the diagonal due to ~ 1 percent ^{13}C in the ^{15}N labelled material. In (B) the chemical structure of tautomers anle138b-*z1* and –*z2* are shown, with the position of two-site ^{13}C labelling indicated in blue. The background shows the approximate size of the molecule in relation to a β-sheet fibril. In (C) 2D ^{15}N-^{13}C TEDOR spectra of Intermediate-I are shown at 1.3 ms (dark blue) and 25 ms (light blue). Dashed lines indicate the positions of anle138b ^{13}C resonances. DNP enhanced MAS NMR experiments (A and C) were recorded at 14.1 T with MAS of 12.5 kHz at 100 K. TEDOR spectra (C) were recorded in 7 days. The room temperature spectrum (A, red) was recorded at 20 T with 17.5 kHz MAS in 24 h, while the DNP spectrum (A, blue) was recorded in 23 h. "*" denotes a spinning sideband. Figs. S14 and S15 show the full spectral width of the DNP spectra of panels (A) and (C). (For interpretation of the references to colour in this figure legend, the reader is referred to the web version of this article.)

for a sample that had a relatively small enhancement factor, and therefore likely underestimates the improvement found with 60 percent glycerol.

To measure the interaction between anle138b and αS, we performed the aggregation protocol described in our previous work [23], but using liposomes with doubly ^{13}C-labelled anle138b and ^{15}N labelled αS. The aggregation was stopped either just after initial ThT fluorescence is observed, namely Intermediate-I, or after complete fibrillization. The ^{13}C resonances of the doubly ^{13}C-labelled anle138b were assigned using a 1.3 ms ^{13}C–^{13}C radiofrequency driven dipolar recoupling (RFDR) [80] spectrum (Fig. 3A). The two peaks at 144 and 152 ppm belong to the nitrogen proximal carbon and are assigned to C_5 of tautomer anle138b-z1 and C_3 of anle138b-*z2* respectively (Fig. 3B). The peak at 99 ppm originates from the protonated carbon of the pyrazole, C_4. The structures of anle138b in Fig. 3B are shown in relation to the size of a β sheet, showing that when the molecule lies perpendicular to the β strands it extends across about 4 β strands. Note that while both spectra were recorded in about one day, only the DNP enhanced spectrum has sufficient sensitivity to clearly identify cross-peaks between C_4 and C_3/C_5.

Fig. 3C shows a zf-TEDOR [68] spectrum of Intermediate-I with a mixing time of 25 ms in which intermolecular contacts are observed between ^{13}C-labelled anle138b and ^{15}N labelled protein. The nitrogen chemical shift of about 120 ppm indicates a backbone interaction, rather than an interaction at the side-chain of lysine or histidine. The TEDOR spectrum is sensitive for distances below about 6 Å [81], placing anle138b in close proximity to the protein backbone. In the 1.3 ms TEDOR spectrum, one-bond correlations to C_α, C′, and Lysine side-chain are observed due to the 1% natural abundance of ^{13}C in the protein. These protein–protein signals have decayed below the noise in the 25 ms spectrum, with the exception of sidechain Asp or Glu carboxyl resonances at 180 ppm. The high intensity of this signal can be explained by an environment with a low proton density, resulting in a long coherence time, as well as few nearby nitrogen spins that would lead to multi-spin terms during TEDOR [65,68]. Since H50 is the only histidine in αS, the intensity of any histidine nitrogen correlations due to natural abundance of ^{15}N are expected to be below the noise. In addition, the nitrogen signal from anle138b (200 ppm) is substantially different from the H50 sidechain nitrogen resonance at about 165–170 ppm (Figs. S12 and S13). This excludes the histidine nitrogen as a possible assignment for the correlations at 200 ppm that are assigned to anle138b.

Using ^{13}C labelling of the protein and ^{15}N labelling of anle138b (Fig. 4), an NHHC spectrum [82] records carbon resonances from the protein that are in close proximity with nitrogen of anle138b. Fig. 4A shows the two tautomers of anle138b with the labelled ^{15}N atoms

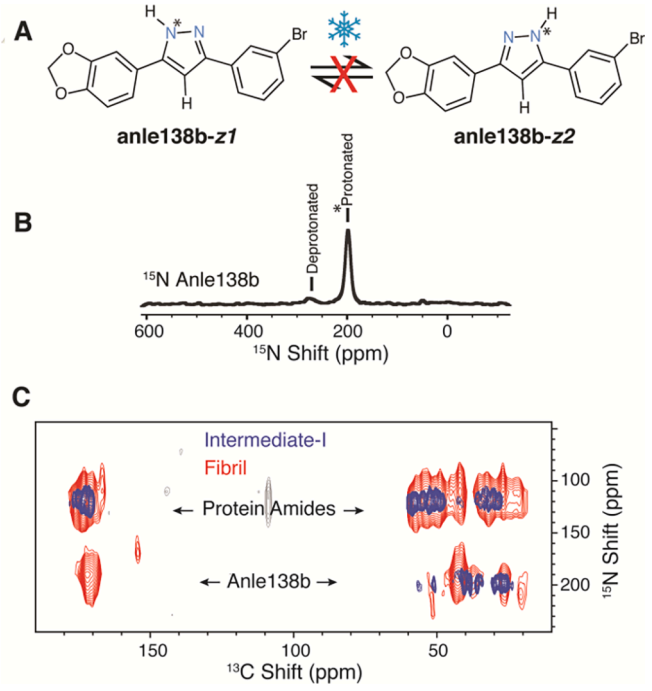

Fig. 4. Anle138b-protein interaction detected for intermediates and fibrils of ^{13}C-labeled αS. In (A), the tautomers of ^{15}N labelled anle138b are depicted. In (B) the 1D ^{15}N spectrum is used to assign the nitrogen resonances of the small molecule to 195 ppm (protonated) and 275 ppm (deprotonated). In (C) the protonated ^{15}N resonance (195 ppm) of anle138b is correlated with ^{13}C resonances of αS for both Intermediate-I (blue) as well as for fibrils (red) in 2D (H) NHHC spectra. Proton-proton mixing was 200 μs. Each spectrum in (C) required 7 days of experimental time. The full NHHC spectra are in Fig. S16. Note that the fibril spectrum is processed with larger line broadening in the ^{15}N dimension such that the peaks are easier to see in the overlay. (For interpretation of the references to colour in this figure legend, the reader is referred to the web version of this article.)

depicted in blue. In Fig. 4B, the 1D ^{15}N spectrum of ^{15}N-labelled anle138b in lipids is shown, allowing assignment of the protonated and deprotonated nitrogen resonances at 195 and 275 ppm respectively. The two protonated (or non-protonated) nitrogen signals of the two tautomers could not be resolved. The ^{15}N-^{13}C NHHC spectrum shows the carbon signals of the protein that are in contact with ^{15}N-labelled anle138b at 195 ppm (protonated nitrogen) for both Intermediate-I and fibril (Fig. 4C). The spectrum of the fibril was reported previously [33]. The backbone C′ resonance at 178 ppm is more prominent in fibrils, as is a resonance at 44 ppm, which was previously assigned to glycine residues in the fibril binding pocket [33]. Assignment of the cross-peaks in Intermediate-I [23], will require additional measurements, for example with amino acid specific labeling. The differences in the spectra, in combination with the fact that the fibril binding pocket has not yet fully formed in Intermediate-I [23], suggests that anle138b may interact with different protein residues in the intermediate.

Rotational Echo Double Resonance (REDOR) spectra [64,83–85] can be used to determine heteronuclear distances between pairs of spins. In the repetitive fibril architecture, REDOR spectra of ^{13}C labelled anle138b are dephased by multiple identical ^{15}N spins of the fibril, even for specifically labeled samples. Fig. 5 and S7 show REDOR dephasing of the ^{13}C labeled anle138b spins due to ^{15}N spins of the protein. The presence of many ^{15}N spins in the protein complicates the analysis of a set of internuclear distances. Nevertheless, considering the variety of possible scenarios discussed in detail in the SI, the labeled $^{13}C_5$ carbon of the central pyrazole ring (144 ppm) of the molecule is located close to the protein. Fit distances are below about 5 Å, and depend on the assumptions about binding (details in the supporting information, Figs. S6 and S7. See also Fig. 6). No matter the fit distance, the REDOR data consistently fit to a stoichiometry of about 1:3 to 1:5 anle138b to αS molecules. This is consistent with the known tubular binding site [33] in which the molecule binds along the fibril axis, the 4.7 Å spacing of parallel β strands,[2] and the 16–17 Å length of anle138b. We recently determined this to be the correct binding site of anle138b in a particular fibril type; the molecule was identified to bind to a tubular cavity within the L2 fibril polymorph [33,86].

The two adjacent ^{13}C labelled pyrazole carbons can be clearly identified in Fig. 5 since the signal is inverted due to the homonuclear *J*-coupling. Nevertheless, quantifying the intensity of these peaks might be impacted by the presence of stronger signals from ^{13}C spins of protein and lipid moieties at 1 percent natural isotopic abundance. Although there is no overlap of the protein or lipid signals with the signals of anle138b at about 99 and 144 ppm, a sideband of the carbonyl resonance centered at 90 ppm is relatively close to the 99-ppm peak, while aromatic resonances are near the 144-ppm peak. These resonances, and even intense resonances such as the carbonyl, could distort the baseline, and impact peak quantitation.

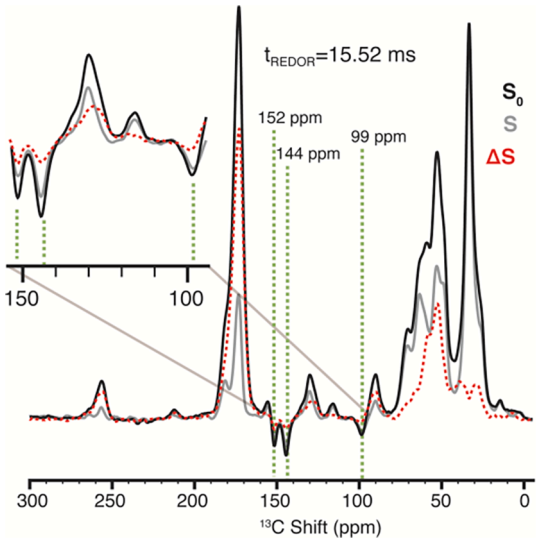

Fig. 5. ^{15}N dephased ^{13}C REDOR spectra at 15.52 ms in αS fibrils. The signals of anle138b (green dashed lines) are negative due to the 1-bond ^{13}C–^{13}C *J*-coupling. The reference S_0 signal is shown in black, the dephased S signal in grey, and the difference, ΔS, is shown as a dashed red line. An expansion of the aromatic region shows negative signals from anle138b. Further details are provided in the SI and Fig. S7. (For interpretation of the references to colour in this figure legend, the reader is referred to the web version of this article.)

To improve the baseline, and to remove the signal modulation due to the homonuclear *J*-coupling, we recorded frequency selective REDOR [69]. Fig. 6A shows the spectrum after 36.8 ms of REDOR dephasing. Fig. 6B shows the REDOR signal as red stars, with a simulated curve shown in black. For the simulation, a set of distances was extracted from an MD simulation snapshot. Seven other snapshots (all 8 used) resulted in similar simulated curves (Fig. S17). The main difference between the simulation curves of different snapshots was a small change in the overall vertical scaling, which is the only fit parameter in Fig. 6. This fit parameter is justified since part of the anle138b population is not bound to fibril and therefore does not dephase. The fit population is consistent with approximately 50% free and 50% bound anle138b, which can be anticipated for saturation of the binding site shown in Fig. 6C. These snapshots contained the molecule in four different orientations in the cavity, as recently described [33]. Specific ^{15}N labeling of the protein could be used in the future to identify the residues responsible for the dephasing in Fig. 6 and thereby refine the binding pose of anle138b. It is also possible that multiple binding poses exist within the cavity. Note that the sample used for this spectrum had 60 % glycerol and 5 mM AMUPol polarizing agent, which resulted in an enhancement factor of about 40 (see Table S3).

Tubular cavities are characteristic of the repetitive fibril architecture and may be unique enough structural features for development of fibril-specific diagnostic molecules. Filling of a tubular cavity in Aβ fibrils by the hydrophobic molecule sulindac sulfide was proposed before [37]. For the lipidic fibril investigated here, a tubular binding site for anle138b was recently identified (Fig. 6C) [33]. For the Intermediate-I, this cavity appears to be partially formed [23], which might explain the differences in the fibril and Intermediate-I resonances observed in contact with the small molecule. Tubular cavities are observed in a variety of fibrils including several other αS polymorphs besides the lipidic fibril investigated here (PDB IDs 8A4L and 8ADS) [86] such as those with the PDB IDs 8A9I [87], 6SSX [3], 6XYO [88], 7NCI [89], 7NCH [89], and 8H03 [90]. They are also found in fibrils of other proteins, such as Tau and Aβ, for example PDB IDs 6NWQ [91] and 6SHS [92]. Fig. 7 shows cross sections (perpendicular to the fibril long axis) of selected polymorphs of αS, tau, and Aβ, each bearing a hydrophobic cavity. These ex-vivo and seeded fibrils were reported by Yang et al. [87] and Fan et al. [90] for the case of Parkinson's disease (PD), Schweighäuser et al. [88] for multiple system atrophy (MSA), Falcon et al. for chronic traumatic encephalopathy (CTE) [91], and Kollmer et al. for Alzheimer's disease (AD) [92]. The expanded view in each case shows a hydrophobic cavity. Note that seeded structures, for example, Lövestam et al. [89] can result in different polymorph as compared with fibrils isolated directly from brain material.

Previous reports linked aggregation intermediates to toxicity and to disruption of membranes via formation of pores [93–95]. Intermediate species have also been determined to contain β-sheet structures [94,96]. Additional details of the structure of such intermediates in complex with molecules such as anle138b are needed to advance our understanding of structure–function relationships. Considering that part of Intermediate-I has formed a fibril-like architecture, it will be particularly interesting to identify the binding site of the small molecule and to compare with the known tubular binding site in lipidic fibrils. With the methods presented here, this is now feasible.

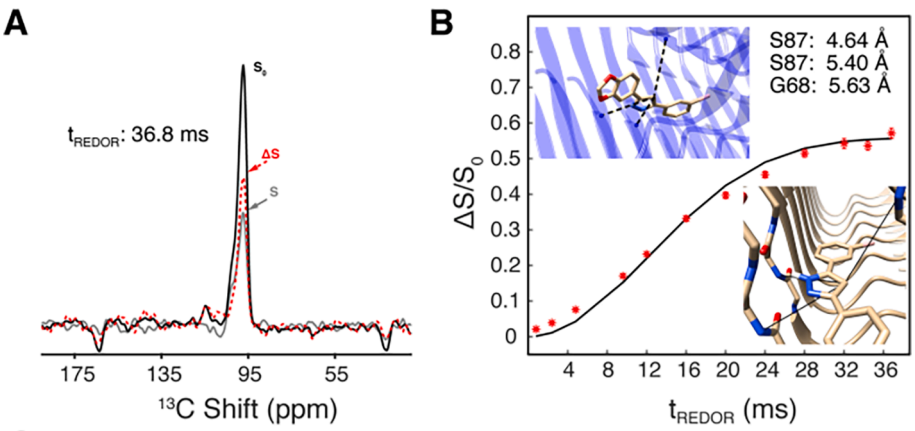

Fig. 6. Frequency selective REDOR spectra dephased by ^{15}N of the protein backbone at 120 ppm and detected at $^{13}C_4$ of anle138b in αS fibrils. In (A) the spectrum at 36.8 ms of REDOR is shown, with the reference S_0 signal in black and the dephased S signal in grey. The difference, ΔS, is shown as a dashed red line. In (B) the simulated signal (black line) fits the observed dephasing curve (red stars) when the fraction of bound anle138b is 0.56. The remaining fraction is assumed not to dephase. Error bars, which mostly overlap with the size of the stars, are estimated from the spectrum noise. The insets show two views of a snapshot from an MD simulation with anle138b in the tubular cavity. The three closest distances are indicated in (B) and by the dashed lines in the insets. Note that S87 is responsible for two of the closest distances due to the stacking of beta strands in the fibril architecture. (C) shows a top-down view of the cavity. (For interpretation of the references to colour in this figure legend, the reader is referred to the web version of this article.)

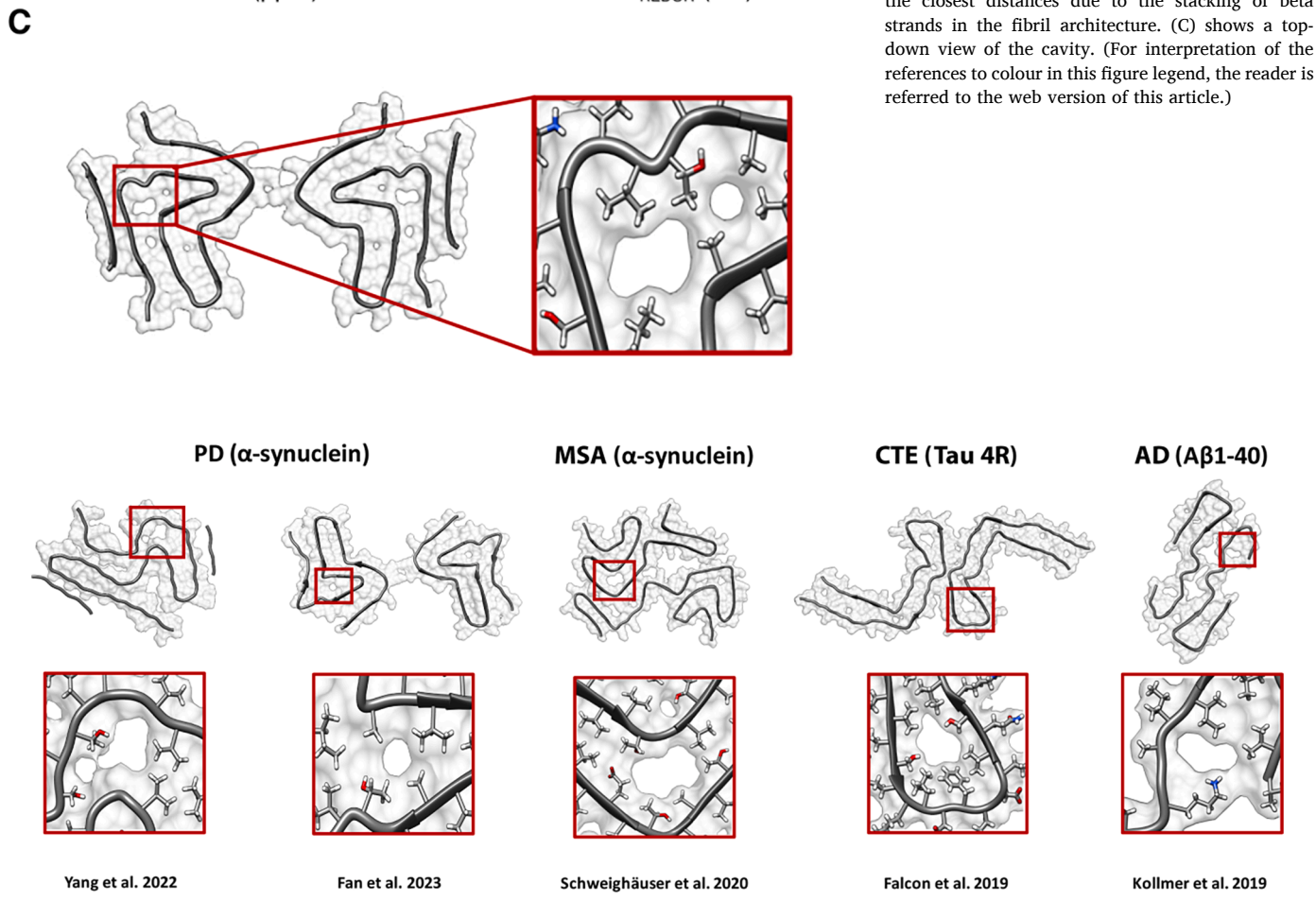

Fig. 7. Selected fibril structures bearing hydrophobic cavities and the associated diseases: an αS fibril of Parkinson's disease (PD) and a fibril seeded from cerebrospinal fluid of a PD patient, an αS fibril of multiple system atrophy (MSA), a Tau fibril of chronic traumatic encephalopathy (CTE) and an Aβ fibril of Alzheimer's disease (AD).

4. Conclusions

In summary, we have shown how DNP enhanced NMR can be applied to detect and characterize binding sites of ^{13}C or ^{15}N labelled small molecules with ^{15}N or ^{13}C labelled amyloid-related intermediates or fibrils in the presence of liposomes. The high sensitivity of DNP enhanced NMR allows the study of such interactions even when they are sub-stoichiometric in the presence of liposomes. Due to the low temperature of 100 K, measurement times can be adapted to accumulate the required signal and are not compromised by the instability of the sample at high temperature.

We showed here how the signal enhancement provided by DNP allows rapid detection of the interaction between protein and small molecule in the αS aggregates. The frequency encoding of NMR signals of both the small molecule, as well as the protein, makes the approach general. For fibrils, this method was used together with amino acid specific labelling to identify a binding site within a tubular cavity.[33] It was also possible to detect an interaction in intermediates, and further measurements will be needed to identify the residues involved in the interaction. As for the fibril, we plan to do this with amino acid specific labelling. Understanding of the binding site (or multiple sites) may require further characterization of the αS Intermediate-I structure, which we are currently pursuing via a combination of DNP and proton-detected NMR.

The same DNP approach can also be applied to other fibril forms of various proteins in the future. These studies might lead to the identification of common structural features that are recognized by anle138b or other fibril-binding molecules. This approach demonstrated on the example of anle138b will be specifically useful for the development of fibril diagnostic compounds usable for example for PET and will complement studies conducted with cryo EM. The short distances observed in fibrils via TEDOR, REDOR, and NHHC spectra establish that the pyrazole moiety of anle138b binds close to the protein backbone for both fibrils and Intermediate-I and entertains side chain contacts. Regarding therapeutic activity targeting intermediates, the methodology presented here appears sufficiently promising to study the activity of anle138b or other therapeutically active molecules with aggregation intermediates that might be modulated in their structure and therefore toxicity due to the small molecule interaction. Such structural insights on a variety of protein sequences will help to explain why anle138b is therapeutically active in mouse models of different diseases linked to aggregation of various protein sequences.

Author contributions

The manuscript was written through contributions of all authors. / All authors have given approval to the final version of the manuscript. / The following contribution list is prepared based on https://casrai.org/credit/

R.D.: data acquisition, analysis, investigation, methodology, validation, visualization, writing - original draft; L.A.: investigation, methodology, resources, visualization, writing - review & editing; E.N.: data acquisition, analysis, and visualization (REDOR data); V.S.: validation (chemical validation of the Intermediate I); M.K.: data acquisition; S.R.: resources (isotopically labelled small molecule); A.L.: resources (isotopically labelled small molecule); J.C.F.: validation (chemical validation of the radical); M.W.: resources (protein synthesis); K.G.: resources (protein synthesis); G.M.: investigation, resources (EPR study of MPI-BPC synthesized radical for DNP) A.G.: resources; S.B.: resources, writing – review & editing; C.G.: conceptualization, funding acquisition, project administration, supervision; L.B.A.: conceptualization, funding acquisition, project administration, supervision, writing original draft. All authors contributed towards review & editing of the final draft.

Author identification by ORCID (https://orcid.org)

R.D.: 0000-0003-0579-9088, L.A.: 0000-0001-9948-7493, E.N.: 0000-0003-3002-0718, V.S.: 0000-0001-7577-4607, M.K.: 0000-0003-0693-3090, S.R.: 0000-0002-2685-7956, A.L.: 0000-0002-5586-9382, J.C.F.: 0000-0003-3239-3868, M.W.: 0000-0002-3249-3917, K.G.: 0000-0002-4149-7899, G.M.: 0000-0002-2719-0743, A.G.: 0000-0002-8238-4102, S.B.: 0000-0003-2041-5740, CG: 0000-0002-1266-4344, L. B.A.: 0000-0003-3216-9065.

Declaration of Competing Interest

The authors declare that they have no known competing financial interests or personal relationships that could have appeared to influence the work reported in this paper. AG, AL, SR and CG are inventors in two patents (USA Pat., US20110293520A1 and Pat. WO 2021/099518) related to the diaryl pyrazole compounds, in particular anle138b. AG and CG are shareholders and co-founders of MODAG GmbH. AG is a full-time employee, AL and SR are part-time employees of MODAG GmbH.

Data availability

Data will be made available on request.

Acknowledgment

We thank Mr. J. Schimpfhauser, Mr. J. Bienert and Dr. V. N. Belov from the facility for Synthetic Chemistry at Max Planck Institute for Multidisciplinary Sciences, Göttingen for synthesizing the TEMTriPol-1 radical and the compound anle138b. We thank Dirk Matthes for supplying MD simulation snapshots. We acknowledge our funding sources, project A04 of the SFB 803 (to L.B.A. and C.G.), the Emmy Noether program (grant AN1316/1-1 to L.B.A.), and Germany's Excellence Strategy (EXC 2067/1- 390729940 to C.G.) of the Deutsche Forschungsgemeinschaft (DFG, German Research Foundation) as well as the Max Planck Society (to C.G.). G.M. was supported by the DFG through an Emmy Noether Grant (project no. 321027114).

Appendix A. Supplementary data

Supplementary data to this article can be found online at https://doi.org/10.1016/j.ymeth.2023.04.002.

References

[1] D. Sulzer, R.H. Edwards, The physiological role of α-synuclein and its relationship to Parkinson's Disease, J. Neurochem. 150 (5) (2019) 475–486.
[2] Sunde, M.; Serpell, L. C.; Bartlam, M.; Fraser, P. E.; Pepys, M. B.; Blake, C. C. F., Common core structure of amyloid fibrils by synchrotron X-ray diffraction11Edited by F. E. Cohen. *Journal of Molecular Biology* **1997,** *273* (3), 729-739.
[3] Guerrero-Ferreira, R.; Taylor, N. M. I.; Arteni, A.-A.; Kumari, P.; Mona, D.; Ringler, P.; Britschgi, M.; Lauer, M. E.; Makky, A.; Verasdonck, J.; Riek, R.; Melki, R.; Meier, B. H.; Böckmann, A.; Bousset, L.; Stahlberg, H., Two new polymorphic structures of human full-length alpha-synuclein fibrils solved by cryo-electron microscopy. *eLife* **2019,** *8*, e48907.
[4] R. Guerrero-Ferreira, N.M.I. Taylor, D. Mona, P. Ringler, M.E. Lauer, R. Riek, M. Britschgi, H. Stahlberg, Cryo-EM structure of alpha-synuclein fibrils, eLife 7 (2018) e36402.
[5] M. Bucciantini, E. Giannoni, F. Chiti, F. Baroni, L. Formigli, J. Zurdo, N. Taddei, G. Ramponi, C.M. Dobson, M. Stefani, Inherent toxicity of aggregates implies a common mechanism for protein misfolding diseases, Nature 416 (6880) (2002) 507–511.
[6] D. Ghosh, P.K. Singh, S. Sahay, N.N. Jha, R.S. Jacob, S. Sen, A. Kumar, R. Riek, S. K. Maji, Structure based aggregation studies reveal the presence of helix-rich intermediate during α-Synuclein aggregation, Sci. Rep. 5 (1) (2015) 9228.
[7] B.S. Gadad, G.B. Britton, K.S. Rao, Targeting Oligomers in Neurodegenerative Disorders: Lessons from α-Synuclein, Tau, and Amyloid-β Peptide, J. Alzheimers Dis. 24 (2011) 223–232.
[8] M.D. Kirkitadze, G. Bitan, D.B. Teplow, Paradigm shifts in Alzheimer's disease and other neurodegenerative disorders: The emerging role of oligomeric assemblies, J. Neurosci. Res. 69 (5) (2002) 567–577.
[9] D.P. Karpinar, M.B.G. Balija, S. Kügler, F. Opazo, N. Rezaei-Ghaleh, N. Wender, H.-Y. Kim, G. Taschenberger, B.H. Falkenburger, H. Heise, A. Kumar, D. Riedel, L. Fichtner, A. Voigt, G.H. Braus, K. Giller, S. Becker, A. Herzig, M. Baldus, H. Jäckle, S. Eimer, J.B. Schulz, C. Griesinger, M. Zweckstetter, Pre-fibrillar α-synuclein variants with impaired β-structure increase neurotoxicity in Parkinson's disease models, EMBO J. 28 (20) (2009) 3256–3268.
[10] G.M. Mohite, A. Navalkar, R. Kumar, S. Mehra, S. Das, L.G. Gadhe, D. Ghosh, B. Alias, V. Chandrawanshi, A. Ramakrishnan, S. Mehra, S.K. Maji, The Familial α-Synuclein A53E Mutation Enhances Cell Death in Response to Environmental Toxins Due to a Larger Population of Oligomers, Biochemistry 57 (33) (2018) 5014–5028.
[11] M. Kostka, T. Högen, K.M. Danzer, J. Levin, M. Habeck, A. Wirth, R. Wagner, C. G. Glabe, S. Finger, U. Heinzelmann, P. Garidel, W. Duan, C.A. Ross, H. Kretzschmar, A. Giese, Single Particle Characterization of Iron-induced Pore-forming α-Synuclein Oligomers*, J. Biol. Chem. 283 (16) (2008) 10992–11003.
[12] M. Bartels, D. Weckbecker, P.-H. Kuhn, S. Ryazanov, A. Leonov, C. Griesinger, S. F. Lichtenthaler, K. Bötzel, A. Giese, Iron-mediated aggregation and toxicity in a novel neuronal cell culture model with inducible alpha-synuclein expression, Sci. Rep. 9 (1) (2019) 9100.
[13] N. Bengoa-Vergniory, R.F. Roberts, R. Wade-Martins, J. Alegre-Abarrategui, Alpha-synuclein oligomers: a new hope, Acta Neuropathol. 134 (6) (2017) 819–838.
[14] K.M. Danzer, D. Haasen, A.R. Karow, S. Moussaud, M. Habeck, A. Giese, H. Kretzschmar, B. Hengerer, M. Kostka, Different Species of α-Synuclein Oligomers Induce Calcium Influx and Seeding, J. Neurosci. 27 (34) (2007) 9220–9232.
[15] H.A. Lashuel, B.M. Petre, J. Wall, M. Simon, R.J. Nowak, T. Walz, P.T. Lansbury, α-Synuclein, Especially the Parkinson's Disease-associated Mutants, Forms Pore-like Annular and Tubular Protofibrils, J. Mol. Biol. 322 (5) (2002) 1089–1102.
[16] F. Schmidt, J. Levin, F. Kamp, H. Kretzschmar, A. Giese, K. Bötzel, Single-Channel Electrophysiology Reveals a Distinct and Uniform Pore Complex Formed by α-Synuclein Oligomers in Lipid Membranes, PLoS One 7 (8) (2012) e42545.
[17] A. Martinez Hernandez, H. Urbanke, A.L. Gillman, J. Lee, S. Ryazanov, H. Y. Agbemenyah, E. Benito, G. Jain, L. Kaurani, G. Grigorian, A. Leonov, N. Rezaei-

Ghaleh, P. Wilken, F.T. Arce, J. Wagner, M. Fuhrman, M. Caruana, A. Camilleri, N. Vassallo, M. Zweckstetter, R. Benz, A. Giese, A. Schneider, M. Korte, R. Lal, C. Griesinger, G. Eichele, A. Fischer, The diphenylpyrazole compound anle138b blocks Aβ channels and rescues disease phenotypes in a mouse model for amyloid pathology, EMBO Mol. Med. 10 (1) (2018) 32–47.
[18] S. Ghio, A. Camilleri, M. Caruana, V.C. Ruf, F. Schmidt, A. Leonov, S. Ryazanov, C. Griesinger, R.J. Cauchi, F. Kamp, A. Giese, N. Vassallo, Cardiolipin Promotes Pore-Forming Activity of Alpha-Synuclein Oligomers in Mitochondrial Membranes, ACS Chem. Nerosci. 10 (8) (2019) 3815–3829.
[19] G. Fusco, S.W. Chen, P.T.F. Williamson, R. Cascella, M. Perni, J.A. Jarvis, C. Cecchi, M. Vendruscolo, F. Chiti, N. Cremades, L. Ying, C.M. Dobson, A. De Simone, Structural basis of membrane disruption and cellular toxicity by α-synuclein oligomers, Science 358 (6369) (2017) 1440.
[20] G. Fusco, A. De Simone, P. Arosio, M. Vendruscolo, G. Veglia, C.M. Dobson, Structural Ensembles of Membrane-bound α-Synuclein Reveal the Molecular Determinants of Synaptic Vesicle Affinity, Sci. Rep. 6 (2016) 27125.
[21] G. Fusco, A. De Simone, T. Gopinath, V. Vostrikov, M. Vendruscolo, C.M. Dobson, G. Veglia, Direct observation of the three regions in α-synuclein that determine its membrane-bound behaviour, Nat. Commun. 5 (1) (2014) 3827.
[22] S. Mehra, S. Sahay, S.K. Maji, α-Synuclein misfolding and aggregation: Implications in Parkinson's disease pathogenesis, Biochimica et Biophysica Acta (BBA) - Proteins and Proteomics 1867 (10) (2019) 890–908.
[23] L. Antonschmidt, R. Dervisoglu, V. Sant, K. Tekwani Movellan, I. Mey, D. Riedel, C. Steinem, S. Becker, L.B. Andreas, C. Griesinger, Insights into the molecular mechanism of amyloid filament formation: Segmental folding of alpha-synuclein on lipid membranes, Sci. Adv. 7 (20) (2021).
[24] ClinicalTrials.gov ClinicalTrials.gov is a database of privately and publicly funded clinical studies conducted around the world. https://clinicaltrials.gov.
[25] Giese, A.; Bertsch, U.; Kretzschmar, H.; Habeck, M.; Hirschberger, T.; Tavan, P.; Griesinger, C.; Leonov, A.; Ryazanov, S.; Weber, P.; Geissen, M.; Groschup, M. H.; Wagner, J. New drug for inhibiting aggregation of proteins involved in diseases linked to protein aggregation and/or neurodegenerative diseases. US20110293520A1, 2011.
[26] J. Wagner, S. Ryazanov, A. Leonov, J. Levin, S. Shi, F. Schmidt, C. Prix, F. Pan-Montojo, U. Bertsch, G. Mitteregger-Kretzschmar, M. Geissen, M. Eiden, F. Leidel, T. Hirschberger, A.A. Deeg, J.J. Krauth, W. Zinth, P. Tavan, J. Pilger, M. Zweckstetter, T. Frank, M. Bähr, J.H. Weishaupt, M. Uhr, H. Urlaub, U. Teichmann, M. Samwer, K. Bötzel, M. Groschup, H. Kretzschmar, C. Griesinger, A. Giese, Anle138b: a novel oligomer modulator for disease-modifying therapy of neurodegenerative diseases such as prion and Parkinson's disease, Acta Neuropathol. 125 (6) (2013) 795–813.
[27] Wegrzynowicz, M.; Bar-On, D.; Calo', L.; Anichtchik, O.; Iovino, M.; Xia, J.; Ryazanov, S.; Leonov, A.; Giese, A.; Dalley, J. W.; Griesinger, C.; Ashery, U.; Spillantini, M. G., Depopulation of dense α-synuclein aggregates is associated with rescue of dopamine neuron dysfunction and death in a new Parkinson's disease model. *Acta Neuropathol.* **2019,** *138* (4), 575-595.
[28] J. Levin, F. Schmidt, C. Boehm, C. Prix, K. Bötzel, S. Ryazanov, A. Leonov, C. Griesinger, A. Giese, The oligomer modulator anle138b inhibits disease progression in a Parkinson mouse model even with treatment started after disease onset, Acta Neuropathol. 127 (5) (2014) 779–780.
[29] A. Heras-Garvin, D. Weckbecker, S. Ryazanov, A. Leonov, C. Griesinger, A. Giese, G.K. Wenning, N. Stefanova, Anle138b modulates alpha-synuclein oligomerization and prevents motor decline and neurodegeneration in a mouse model of multiple system atrophy, Mov. Disord. 34 (2) (2019) 255–263.
[30] J. Wagner, S. Krauss, S. Shi, S. Ryazanov, J. Steffen, C. Miklitz, A. Leonov, A. Kleinknecht, B. Göricke, J.H. Weishaupt, D. Weckbecker, A.M. Reiner, W. Zinth, J. Levin, D. Ehninger, S. Remy, H.A. Kretzschmar, C. Griesinger, A. Giese, M. Fuhrmann, Reducing tau aggregates with anle138b delays disease progression in a mouse model of tauopathies, Acta Neuropathol. 130 (5) (2015) 619–631.
[31] M. Brendel, M. Deussing, T. Blume, L. Kaiser, F. Probst, F. Overhoff, F. Peters, B. von Ungern-Sternberg, S. Ryazanov, A. Leonov, C. Griesinger, A. Zwergal, J. Levin, P. Bartenstein, I. Yakushev, P. Cumming, G. Boening, S. Ziegler, J. Herms, A. Giese, A. Rominger, Late-stage Anle138b treatment ameliorates tau pathology and metabolic decline in a mouse model of human Alzheimer's disease tau, Alzheimers Res. Ther. 11 (1) (2019) 67.
[32] D. Matthes, V. Gapsys, C. Griesinger, B.L. de Groot, Resolving the Atomistic Modes of Anle138b Inhibitory Action on Peptide Oligomer Formation, ACS Chem. Nerosci. 8 (12) (2017) 2791–2808.
[33] L. Antonschmidt, D. Matthes, R. Dervisoglu, B. Frieg, C. Dienemann, A. Leonov, E. Nimerovsky, V. Sant, S. Ryazanov, A. Giese, G.F. Schroder, S. Becker, B.L. de Groot, C. Griesinger, L.B. Andreas, The clinical drug candidate anle138b binds in a cavity of lipidic alpha-synuclein fibrils, Nat. Commun. 13 (1) (2022) 5385.
[34] C. Gowda, G. Zandomeneghi, H. Zimmermann, A.K. Schütz, A. Böckmann, M. Ernst, B.H. Meier, The conformation of the Congo-red ligand bound to amyloid fibrils HET-s(218–289): a solid-state NMR study, J. Biomol. NMR 69 (4) (2017) 207–213.
[35] A.K. Schütz, A. Soragni, S. Hornemann, A. Aguzzi, M. Ernst, A. Böckmann, B. H. Meier, The Amyloid-Congo Red Interface at Atomic Resolution, Angew. Chem. Int. Ed. 50 (26) (2011) 5956–5960.
[36] Z. Niu, R. Sarkar, M. Aichler, H.-J. Wester, B.H. Yousefi, B. Reif, Mapping the Binding Interface of PET Tracer Molecules and Alzheimer Disease Aβ Fibrils by Using MAS Solid-State NMR Spectroscopy, Chembiochem 21 (17) (2020) 2495–2502.
[37] E. Prade, H.J. Bittner, R. Sarkar, J.M. Lopez del Amo, G. Althoff-Ospelt, G. Multhaup, P.W. Hildebrand, B. Reif, Structural Mechanism of the Interaction of Alzheimer Disease Aβ Fibrils with the Non-steroidal Anti-inflammatory Drug (NSAID) Sulindac Sulfide, J. Biol. Chem. 290 (48) (2015) 28737–28745.
[38] M. Goedert, Y. Yamaguchi, S.K. Mishra, M. Higuchi, N. Sahara, Tau Filaments and the Development of Positron Emission Tomography Tracers, Front. Neurol. 9 (70) (2018).
[39] P.M. Seidler, K.A. Murray, D.R. Boyer, P. Ge, M.R. Sawaya, C.J. Hu, X. Cheng, R. Abskharon, H. Pan, M.A. DeTure, C.K. Williams, D.W. Dickson, H.V. Vinters, D. S. Eisenberg, Structure-based discovery of small molecules that disaggregate Alzheimer's disease tissue derived tau fibrils in vitro, Nat. Commun. 13 (1) (2022) 5451.
[40] A.A. Deeg, A.M. Reiner, F. Schmidt, F. Schueder, S. Ryazanov, V.C. Ruf, K. Giller, S. Becker, A. Leonov, C. Griesinger, A. Giese, W. Zinth, Anle138b and related compounds are aggregation specific fluorescence markers and reveal high affinity binding to α-synuclein aggregates, Biochim. Biophys. Acta Gen. Subj. 1850 (9) (2015) 1884–1890.
[41] A.M. Reiner, F. Schmidt, S. Ryazanov, A. Leonov, D. Weckbecker, A.A. Deeg, C. Griesinger, A. Giese, W. Zinth, Photophysics of diphenyl-pyrazole compounds in solutions and α-synuclein aggregates, Biochim. Biophys. Acta Gen. Subj. 1862 (4) (2018) 800–807.
[42] A.K. Schütz, S. Hornemann, M.A. Wälti, L. Greuter, C. Tiberi, R. Cadalbert, M. Gantner, R. Riek, P. Hammarström, K.P.R. Nilsson, A. Böckmann, A. Aguzzi, B. H. Meier, Binding of Polythiophenes to Amyloids: Structural Mapping of the Pharmacophore, ACS Chem. Nerosci. 9 (3) (2018) 475–481.
[43] M. Groenning, Binding mode of Thioflavin T and other molecular probes in the context of amyloid fibrils-current status, J. Chem. Biol. 3 (1) (2010) 1–18.
[44] M.R. Krebs, E.H. Bromley, A.M. Donald, The binding of thioflavin-T to amyloid fibrils: localisation and implications, J Struct Biol 149 (1) (2005) 30–37.
[45] L.B. Andreas, A.B. Barnes, B. Corzilius, J.J. Chou, E.A. Miller, M. Caporini, M. Rosay, R.G. Griffin, Dynamic Nuclear Polarization Study of Inhibitor Binding to the M218–60 Proton Transporter from Influenza A, Biochemistry 52 (16) (2013) 2774–2782.
[46] A.B. Barnes, G. De Paëpe, P.C.A. van der Wel, K.N. Hu, C.G. Joo, V.S. Bajaj, M. L. Mak-Jurkauskas, J.R. Sirigiri, J. Herzfeld, R.J. Temkin, R.G. Griffin, High-Field Dynamic Nuclear Polarization for Solid and Solution Biological NMR, Appl. Magn. Reson. 34 (3) (2008) 237–263.
[47] A. König, D. Schölzel, B. Uluca, T. Viennet, Ü. Akbey, H. Heise, Hyperpolarized MAS NMR of unfolded and misfolded proteins, Solid State Nucl. Magn. Reson. 98 (2019) 1–11.
[48] B. Uluca, T. Viennet, D. Petrović, H. Shaykhalishahi, F. Weirich, A. Gönülalan, B. Strodel, M. Etzkorn, W. Hoyer, H. Heise, DNP-Enhanced MAS NMR: A Tool to Snapshot Conformational Ensembles of α-Synuclein in Different States, Biophys. J. 114 (7) (2018) 1614–1623.
[49] M. Rosay, A.-C. Zeri, N.S. Astrof, S.J. Opella, J. Herzfeld, R.G. Griffin, Sensitivity-Enhanced NMR of Biological Solids: Dynamic Nuclear Polarization of Y21M fd Bacteriophage and Purple Membrane, J. Am. Chem. Soc. 123 (5) (2001) 1010–1011.
[50] D.A. Hall, D.C. Maus, G.J. Gerfen, S.J. Inati, L.R. Becerra, F.W. Dahlquist, R. G. Griffin, Polarization-Enhanced NMR Spectroscopy of Biomolecules in Frozen Solution, Science 276 (5314) (1997) 930–932.
[51] F. Mentink-Vigier, G. Mathies, Y. Liu, A.-L. Barra, M.A. Caporini, D. Lee, S. Hediger, G. Griffin, R., De Paëpe, G.,, Efficient cross-effect dynamic nuclear polarization without depolarization in high-resolution MAS NMR, Chem. Sci. (2017).
[52] G. Mathies, M.A. Caporini, V.K. Michaelis, Y. Liu, K.-N. Hu, D. Mance, J.L. Zweier, M. Rosay, M. Baldus, R.G. Griffin, Efficient Dynamic Nuclear Polarization at 800 MHz/527 GHz with Trityl-Nitroxide Biradicals, Angew. Chem. Int. Ed. 54 (40) (2015) 11770–11774.
[53] X. Cai, A. Lucini Paioni, A. Adler, R. Yao, W. Zhang, D. Beriashvili, A. Safeer, A. Gurinov, A. Rockenbauer, Y. Song, M. Baldus, Y. Liu, Highly Efficient Trityl-Nitroxide Biradicals for Biomolecular High-Field Dynamic Nuclear Polarization, Chemistry 27 (50) (2021) 12758–12762.
[54] N.T. Tran, F. Mentink-Vigier, J.R. Long, Dynamic Nuclear Polarization of Biomembrane Assemblies, Biomolecules 10 (9) (2020).
[55] B. Corzilius, L.B. Andreas, A.A. Smith, Q.Z. Ni, R.G. Griffin, Paramagnet induced signal quenching in MAS–DNP experiments in frozen homogeneous solutions, J. Magn. Reson. 240 (2014) 113–123.
[56] D. Lacabanne, M.-L. Fogeron, T. Wiegand, R. Cadalbert, B.H. Meier, A. Böckmann, Protein sample preparation for solid-state NMR investigations, Prog. Nucl. Magn. Reson. Spectrosc. 110 (2019) 20–33.
[57] C. Gardiennet, A.K. Schütz, A. Hunkeler, B. Kunert, L. Terradot, A. Böckmann, B. H. Meier, A Sedimented Sample of a 59 kDa Dodecameric Helicase Yields High-Resolution Solid-State NMR Spectra, Angew. Chem. Int. Ed. 51 (31) (2012) 7855–7858.
[58] B.M. Fung, A.K. Khitrin, K. Ermolaev, An Improved Broadband Decoupling Sequence for Liquid Crystals and Solids, J. Magn. Reson. 142 (1) (2000) 97–101.
[59] L. Emsley G. Bodenhausen Optimization of shaped selective pulses for NMR using a quaternion description of their overall propagators Journal of Magnetic Resonance 97 1 (1969) 1992, 135 148.
[60] Y. Liu, F.A. Villamena, A. Rockenbauer, Y. Song, J.L. Zweier, Structural Factors Controlling the Spin-Spin Exchange Coupling: EPR Spectroscopic Studies of Highly Asymmetric Trityl-Nitroxide Biradicals, J. Am. Chem. Soc. 135 (6) (2013) 2350–2356.
[61] D.H. Zhou, C.M. Rienstra, High-performance solvent suppression for proton detected solid-state NMR, J. Magn. Reson. 192 (1) (2008) 167–172. San Diego, Calif. : 1997.
[62] C. Vinod Chandran, P.K. Madhu, N.D. Kurur, T. Bräuniger, Swept-frequency two-pulse phase modulation (SWf-TPPM) sequences with linear sweep profile for

heteronuclear decoupling in solid-state NMR, Magnetic resonance in chemistry : MRC 46 (10) (2008) 943–947.
[63] A.J. Shaka J. Keeler T. Frenkiel R. Freeman An improved sequence for broadband decoupling: WALTZ-16 Journal of Magnetic Resonance 52 2 (1969) 1983, 335 338.
[64] T. Gullion J. Schaefer Rotational-echo double-resonance NMR Journal of Magnetic Resonance 81 1 (1969) 1989, 196 200.
[65] X.C. Zhang, M.C. Forster, E. Nimerovsky, K.T. Movellan, L.B. Andreas, Transferred-Rotational-Echo Double Resonance, Chem. A Eur. J. 125 (3) (2021) 754–769.
[66] E. Nimerovsky, K.T. Movellan, X.C. Zhang, M.C. Forster, E. Najbauer, K. Xue, R. Dervisoglu, K. Giller, C. Griesinger, S. Becker, L.B. Andreas, Proton Detected Solid-State NMR of Membrane Proteins at 28 Tesla (1.2 GHz) and 100 kHz Magic-Angle Spinning, Biomolecules 11 (5) (2021) 752.
[67] R.R. Ernst, G. Bodenhausen, A. Wokaun, Principles of Nuclear Magnetic Resonance in One and Two Dimensions, Clarendon Press, Oxford, UK, 1987.
[68] C.P. Jaroniec, C. Filip, R.G. Griffin, 3D TEDOR NMR Experiments for the Simultaneous Measurement of Multiple Carbon−Nitrogen Distances in Uniformly 13C,15N-Labeled Solids, J. Am. Chem. Soc. 124 (36) (2002) 10728–10742.
[69] C.P. Jaroniec, B.A. Tounge, J. Herzfeld, R.G. Griffin, Frequency selective heteronuclear dipolar recoupling in rotating solids: accurate (13)C-(15)N distance measurements in uniformly (13)C, (15)N-labeled peptides, J Am Chem Soc 123 (15) (2001) 3507–3519.
[70] S.Y. Liao, M. Lee, T. Wang, I.V. Sergeyev, M. Hong, Efficient DNP NMR of membrane proteins: sample preparation protocols, sensitivity, and radical location, J. Biomol. NMR 64 (3) (2016) 223–237.
[71] C. Sauvée, M. Rosay, G. Casano, F. Aussenac, R.T. Weber, O. Ouari, P. Tordo, Highly Efficient, Water-Soluble Polarizing Agents for Dynamic Nuclear Polarization at High Frequency, Angew. Chem. Int. Ed. 52 (41) (2013) 10858–10861.
[72] K.R. Thurber, R. Tycko, Perturbation of nuclear spin polarizations in solid state NMR of nitroxide-doped samples by magic-angle spinning without microwaves, J. Chem. Phys. 140 (18) (2014), 184201.
[73] F. Mentink-Vigier, Ü. Akbey, H. Oschkinat, S. Vega, A. Feintuch, Theoretical aspects of Magic Angle Spinning - Dynamic Nuclear Polarization, J. Magn. Reson. 258 (2015) 102–120.
[74] D. Lee, S. Hediger, G. De Paëpe, Is solid-state NMR enhanced by dynamic nuclear polarization? Solid State Nucl. Magn. Reson. 66–67 (2015) 6–20.
[75] F. Mentink-Vigier, S. Paul, D. Lee, A. Feintuch, S. Hediger, S. Vega, G. De Paëpe, Nuclear depolarization and absolute sensitivity in magic-angle spinning cross effect dynamic nuclear polarization, PCCP 17 (34) (2015) 21824–21836.
[76] W. Zhai, A. Lucini Paioni, X. Cai, S. Narasimhan, J. Medeiros-Silva, W. Zhang, A. Rockenbauer, M. Weingarth, Y. Song, M. Baldus, Y. Liu, Postmodification via Thiol-Click Chemistry Yields Hydrophilic Trityl-Nitroxide Biradicals for Biomolecular High-Field Dynamic Nuclear Polarization, J Phys Chem B 124 (41) (2020) 9047–9060.
[77] P.C. van der Wel, K.N. Hu, J. Lewandowski, R.G. Griffin, Dynamic nuclear polarization of amyloidogenic peptide nanocrystals: GNNQQNY, a core segment of the yeast prion protein Sup35p, J Am Chem Soc 128 (33) (2006) 10840–10846.
[78] Giese, A.; Schmidt, F.; Weckbecker, D.; Leonov, A.; Ryazanov, S.; Griesinger, C.; Pichler, B. J.; Herfert, K.; Maurer, A.; Kübler, L.; Buss, S. Novel compounds for the diagnosis, treatment and prevention of diseases associated with the aggregation of alpha-synuclein. WO 2021/099518 (A1), 2021.
[79] L. Kuebler, S. Buss, A. Leonov, S. Ryazanov, F. Schmidt, A. Maurer, D. Weckbecker, A.M. Landau, T.P. Lillethorup, D. Bleher, R.S. Saw, B.J. Pichler, C. Griesinger, A. Giese, K. Herfert, [(11)C]MODAG-001-towards a PET tracer targeting alpha-synuclein aggregates, Eur J Nucl Med Mol Imaging 48 (6) (2021) 1759–1772.
[80] A.E. Bennett, C.M. Rienstra, J.M. Griffiths, W. Zhen, P.T. Lansbury, R.G. Griffin, Homonuclear radio frequency-driven recoupling in rotating solids, J. Chem. Phys. 108 (22) (1998) 9463–9479.
[81] A.A. Shcherbakov, J. Medeiros-Silva, N. Tran, M.D. Gelenter, M. Hong, From Angstroms to Nanometers: Measuring Interatomic Distances by Solid-State NMR, Chem. Rev. (2021).
[82] A. Lange, S. Luca, M. Baldus, Structural Constraints from Proton-Mediated Rare-Spin Correlation Spectroscopy in Rotating Solids, J. Am. Chem. Soc. 124 (33) (2002) 9704–9705.
[83] C.P. Jaroniec, B.A. Tounge, C.M. Rienstra, J. Herzfeld, R.G. Griffin, Measurement of 13C–15N Distances in Uniformly 13C Labeled Biomolecules: J-Decoupled REDOR, J. Am. Chem. Soc. 121 (43) (1999) 10237–10238.
[84] T. Gullion, Rotational-Echo, Double-Resonance NMR, in: G.A. Webb (Ed.), Modern Magnetic Resonance, Springer Science & Business Media, Berlin, 2006, pp. 713–718.
[85] J.M. Goetz, J. Schaefer, REDOR Dephasing by Multiple Spins in the Presence of Molecular Motion, J. Magn. Reson. 127 (2) (1997) 147–154.
[86] B. Frieg, L. Antonschmidt, C. Dienemann, J.A. Geraets, E.E. Najbauer, D. Matthes, B.L. de Groot, L.B. Andreas, S. Becker, C. Griesinger, G.F. Schroder, The 3D structure of lipidic fibrils of alpha-synuclein, Nat Commun 13 (1) (2022) 6810.
[87] Y. Yang, Y. Shi, M. Schweighauser, X. Zhang, A. Kotecha, A.G. Murzin, H. J. Garringer, P.W. Cullinane, Y. Saito, T. Foroud, T.T. Warner, K. Hasegawa, R. Vidal, S. Murayama, T. Revesz, B. Ghetti, M. Hasegawa, T. Lashley, S.H. W. Scheres, M. Goedert, Structures of alpha-synuclein filaments from human brains with Lewy pathology, Nature 610 (7933) (2022) 791–795.
[88] M. Schweighauser, Y. Shi, A. Tarutani, F. Kametani, A.G. Murzin, B. Ghetti, T. Matsubara, T. Tomita, T. Ando, K. Hasegawa, S. Murayama, M. Yoshida, M. Hasegawa, S.H.W. Scheres, M. Goedert, Structures of alpha-synuclein filaments from multiple system atrophy, Nature 585 (7825) (2020) 464–469.
[89] S. Lovestam, M. Schweighauser, T. Matsubara, S. Murayama, T. Tomita, T. Ando, K. Hasegawa, M. Yoshida, A. Tarutani, M. Hasegawa, M. Goedert, S.H.W. Scheres, Seeded assembly in vitro does not replicate the structures of alpha-synuclein filaments from multiple system atrophy, FEBS Open Bio 11 (4) (2021) 999–1013.
[90] Y. Fan, Y. Sun, W. Yu, Y. Tao, W. Xia, Y. Liu, Q. Zhao, Y. Tang, Y. Sun, F. Liu, Q. Cao, J. Wu, C. Liu, J. Wang, D. Li, Conformational change of alpha-synuclein fibrils in cerebrospinal fluid from different clinical phases of Parkinson's disease, Structure 31 (1) (2023) 78–87 e5.
[91] B. Falcon, J. Zivanov, W. Zhang, A.G. Murzin, H.J. Garringer, R. Vidal, R. A. Crowther, K.L. Newell, B. Ghetti, M. Goedert, S.H.W. Scheres, Novel tau filament fold in chronic traumatic encephalopathy encloses hydrophobic molecules, Nature 568 (7752) (2019) 420–423.
[92] M. Kollmer, W. Close, L. Funk, J. Rasmussen, A. Bsoul, A. Schierhorn, M. Schmidt, C.J. Sigurdson, M. Jucker, M. Fandrich, Cryo-EM structure and polymorphism of A beta amyloid fibrils purified from Alzheimer's brain tissue. *Nature*, Communications (2019) 10.
[93] H.Y. Kim, M.K. Cho, A. Kumar, E. Maier, C. Siebenhaar, S. Becker, C.O. Fernandez, H.A. Lashuel, R. Benz, A. Lange, M. Zweckstetter, Structural properties of pore-forming oligomers of alpha-synuclein, J Am Chem Soc 131 (47) (2009) 17482–17489.
[94] S. Chimon, M.A. Shaibat, C.R. Jones, D.C. Calero, B. Aizezi, Y. Ishii, Evidence of fibril-like beta-sheet structures in a neurotoxic amyloid intermediate of Alzheimer's beta-amyloid, Nat Struct Mol Biol 14 (12) (2007) 1157–1164.
[95] L. Tosatto, A.O. Andrighetti, N. Plotegher, V. Antonini, I. Tessari, L. Ricci, L. Bubacco, M. Dalla Serra, Alpha-synuclein pore forming activity upon membrane association, Biochim Biophys Acta 1818 (11) (2012) 2876–2883.
[96] D.P. Hong, A.L. Fink, V.N. Uversky, Structural Characteristics of alpha-Synuclein Oligomers Stabilized by the Flavonoid Baicalein, J. Mol. Biol. 383 (1) (2008) 214–223.